Chalcogenide BaZrS3 perovskite solar cells: A numerical simulation and analysis using SCAPS-1D

S. Karthick, S. Velumani, Johann Bouclé

Version of Record: https://www.sciencedirect.com/science/article/pii/S0925346722002841
Manuscript_5853eda7d6f2ff2c83a62af9f0312add

Chalcogenide $BaZrS_3$ perovskite solar cells: A numerical simulation and analysis using SCAPS-1D

S. Karthick[a,b,*], S. Velumani[c,d,*], J. Bouclé[a,*]

(a) Univ. Limoges, CNRS, XLIM, UMR 7252, F-87000 Limoges, France.

(b) Nanoscience and Nanotechnology Program, (c) Department of Electrical Engineering (SEES), Centro de Investigación y de Estudios Avanzados del Instituto Politécnico Nacional (CINVESTAV-IPN), Col. San Pedro Zacatenco, Ciudad de México, 07360.

(d) J. Mike Walker '66 Department of Mechanical Engineering, Texas A & M University, College Station, Texas, 77843, USA.

ABSTRACT

Chalcogenide perovskites (CPs), especially Barium Zirconium Sulfide ($BaZrS_3$), have attracted tremendous attention as a potential alternative to hybrid halide perovskites for optoelectronics due to their exceptional visible light absorption and extraordinary chemical stability. Therefore, we numerically investigated a highly efficient n-i-p CPs model solar cells using the Solar cell simulator capacitance software (SCAPS-1D), consisting of a conventional (i.e., $BaZrS_3$ – 1.9 eV), as well as Ti and S, incorporated absorbers (i.e., $Ba(Zr_{0.95}Ti_{0.05})S_3$ – 1.63 eV and $BaZr(S_{0.6}Se_{0.4})_3$ – 1.76 eV). The systematic studies explored the varying CPs absorber layer properties, the effects of thickness, total and interface (i.e., ETL/CPs and CPs/HTL) defect densities and optimized parameters for ideal device performance. The optimized solar cell parameters yielded a power conversion efficiency (PCE) of 12.42% for $BaZrS_3$, 18.85% for $Ba(Zr_{0.95}Ti_{0.05})S_3$ and 15.47% for $BaZr(S_{0.6}Se_{0.4})_3$ devices, respectively. The study also explored some effects limiting device performance (i.e., interface and surface states) and resultant current leakages or charge recombination, leading to parasitic resistances (R_{Series} and R_{Shunt}). The quantification of the influence of parasitic resistances and working temperatures provided some insight into the device performance, which appear to be reduced with increasing operating temperature and series resistances. These results suggest that chalcogenide $BaZrS_3$ - based perovskites can play a major role as absorber materials towards highly efficient and cheap perovskite solar cells with low environmental impact.

Keywords: SCAPS-1D, Chalcogenide $BaZrS_3$, Perovskite solar cells, defect density, parasitic resistances.

1. Introduction

In a short period of time, organic-inorganic lead halide hybrid perovskite solar cells (PSCs) showed a remarkable power conversion efficiency (PCE) of 25.8% compared to other semiconductor-based devices [1]. At the same time, the presence of toxic lead (Pb) in the material composition, as well as instability issues induced by moisture, heat, light or applied electric field,

restricts their commercialization and leads to pursue the effort towards alternative solar cell materials.

Chalcogenide perovskites (CPs) have recently emerged as a promising environmental-friendly, non-toxic semiconductor material and gained significant attention due to their excellent optoelectronic properties [2]. The CPs material has the general formula of ABX_3, where A = group II cation (i.e., Ca^{2+}, Sr^{2+}, Ba^{2+}), B = group IV transition metals (i.e., Ti^{4+}, Zr^{4+}, Hf^{4+}), and X = chalcogen anions (i.e., S^{2-}, Se^{2-}), respectively. Previous studies showed that the barium zirconium sulfide ($BaZrS_3$), Strontium zirconium sulfide ($SrZrS_3$), Barium Hafnium sulfide ($BaHfS_3$), Strontium Hafnium sulfide ($SrHfS_3$), Calcium zirconium sulfide ($CaZrS_3$) and Calcium Hafnium sulfide ($CaHfS_3$) CPs have a perovskite-type structure with an appropriate band-gap well fitted for Photovoltaic (PV) applications [3–6]. Among these, $BaZrS_3$ CPs have been the most studied compound from the experimental point of view due to their Pb-free nature and superior environmental stability [7–10]. Moreover, it exhibits a large absorption coefficient (> 10^5 cm^{-1}), high tolerance to defects, and excellent carrier mobility, among other specific features [9]. Y. Nishigaki *et al.'s* results clearly demonstrated that the absorption coefficient (α) of CPs are extremely extraordinary compared with all the other practical solar cell absorbers such as GaAs, $CuInSe_2$, $MAPbI_3$, including InP, CdTe, $Cu_2ZnSnSe_4$, and Cu_2ZnSnS_4. Because of the strong band-edge absorption of α, $BaZrS_3$ offers a more accessible collection of photo-generated carriers due to the small light penetration depth (~ 100 nm) [5]. However, the ~ 1.7 – 1.9 eV band-gap of $BaZrS_3$ CPs is slightly higher than the ideal band-gap required for single-junction devices. According to the reported results, alloying, especially through Ti substitution on the Zr site and Se incorporation with S site, can significantly tune the band-gap, which is highly beneficial to fabricate single-junction PV devices [4,5,11]. More importantly, Ti and Se substitution only diminish the band-gap (from 1.9 to 1.75 eV), and it does not largely affect the higher absorption coefficient. CPs generally have p-d transitions, which have a superior joint density of states than p-p transitions that are usually noticed in lead halide perovskites. Therefore, the optical absorption coefficient of CPs is higher compared to lead halide perovskites. As a result, CPs solar cells should be able to use even lighter absorbers to attain higher efficiencies compared to conventional lead halide perovskites [4]. M. Kumar *et al.* theoretically studied the excitonic properties of CPs, and their findings show that the exciton binding energy (E_B) is higher compared to the conventional halide perovskites. Furthermore, the calculated spectroscopic limited maximum efficiency (SLME) results (i.e., based on Eg and α) prove that the CPs are highly suitable for use as an absorber material [12].

In general, a high temperature (> 600° C) is required to achieve crystalline $BaZrS_3$ CPs thin films, which is a major problem in fabricating single or multi-junction solar cells. Using physical deposition methods (i.e., pulsed lased deposition, DC sputtering) or chemical sulfurization of thin films (i.e., $BaZrO_3$), a temperature of almost 700° C to 1000° C can be needed to demonstrate CPs thin films of desired quality, and the obtained CPs compositions contain impurity phases [7–9]. In consequence, low-temperature processes are crucial to fabricate solar devices at low costs, presenting the desired properties (in the bulk and at the interfaces). It is also very complex to

process $BaZrS_3$ CPs thin films from solution as no solvent can be compatible with the necessary high temperatures required for $BaZrS_3$ synthesis. However, V.K. Ravi *et al.* recently used a two-step process to achieve solution-processed 50 nm thick $BaZrS_3$ CPs thin films. Initially, the author synthesized $BaZrS_3$ nanocrystals (NCs) at 600° C, adopting a solid-state synthesis route. Then, they functionalized the $BaZrS_3$ NCs surface to achieve a colloidal dispersion either in N-methyl-2-pyrrolidinone (polar solvent) or in chloroform (non-polar solvent) [13]. Z. Yu *et al.* reports low-temperature (i.e., at 500° C) $BaZrS_3$ CPs thin films by changing the chemical reaction pathway. These results demonstrated that a lower temperature reduces sulfur vacancies and carbon impurities associated with the higher temperature process [10]. Therefore, both publications are opening some paths for the scientific community to synthesize $BaZrS_3$ CPs thin films at low temperatures, giving some promises for potential single or multi-junction solar device fabrication.

Numerical or theoretical tools are regularly exploited to explore potential single- or multiple-junction devices and probe new possible device architectures and combinations. Basically, SCAPS is a one-dimensional simulation software used to design thin-film solar cell structures using many semiconductor layers, and it entirely depends on the optical properties/parameters of the chosen material. The SCAPS program can solve the basic semiconductor equations, such as the Poisson equation and continuity equations with the drift-diffusion approximation. It simulates electrical parameters of solar cells such as the current-voltage curve, quantum efficiency, etc. SCAPS was originally proposed to study CIGS or CdTe type solar cells, and indeed it also operates well for such structures, even with parameters that are very different from CdTe or CIGS. Nowadays, it has been successfully applied to CZTS, perovskite, c-Si, a-Si, and bulk heterojunction solar cell structures. *(SCAPS basic manual.pdf, most recent version).* Moreover, many groups already used the SCAPS software to construct the new device configuration employing new absorber material, such as Antimony selenide (Sb_2Se_3) and antimony sulfide (Sb_2S_3) [14–17], Cu_2XSnS_4 (X = Fe, Mg, Mn, Ni, Sr) [18], Tungsten diselenide (WSe_2) [19], Tin Sulfide (SnS) [20], C_2N [21], Copper bismuth sulfide (Cu_3BiS_3) [22], Bismuth iodide (BiI_3) [23], PBDB-T/ITIC [24], La_2NiMnO_6 (LNMO), Eu_2NiMnO_6 (ENMO) & Dy_2NiMnO_6 (DNMO) [25] and different perovskite materials ($FAPbI_3$ [26], $FASnI_3$ [27], $MAPbI_3$ [28], $MASnI_3$ [29], $MASnBr_3$ [30], $CsPbI_3$ [31], $CsPbBr_3$ [32], Cs_2SnI_6 [33], Cs_2TiBr_6 [34], $CsGeI_3$ [35], $Cs_2AuBiCl_6$ [36], $Cs_4CuSb_2Cl_{12}$ [37], $(FA)_2BiCuI_6$ [38], etc.). In many cases, the simulated results are significantly reliable to the experimental results [22,26,39–43], and of course, the simulations are useful to the solar cell community people. In this context, this study provides a systematic and complete simulation based on CPs (i.e., $BaZrS_3$, $Ba(Zr_{0.95}Ti_{0.05})S_3$ and $BaZr(S_{0.6}Se_{0.4})_3$) used as solar cell absorbers using solar cell simulator capacitance software (SCAPS-1D). Firstly, we construct an ideal n-i-p planar CPs device (i.e., FTO/TiO_2/CPs/Cu_2O/Au), which do not account for series or shunt resistance. Later, the systematic studies show that while varying CPs absorber layer properties, such as the absorber thickness, total (i.e., N_t) and interface (i.e., ETL/CPs and CPs/HTL) defect densities, device performance is drastically influenced. We finally explore the influence of parasitic resistances (R_{Series} and R_{Shunt}) and working temperature over the final

optimized device, as a preliminary step to evaluate the operation of potential CP-based single-junction devices.

2. Device structure and simulation methodology

In this study, CPs-based n-i-p planar perovskite device models (FTO/TiO_2/CPs (i.e., $BaZrS_3$, $Ba(Zr_{0.95}Ti_{0.05})S_3$, $BaZr(S_{0.6}Se_{0.4})_3$)/Cu_2O/Au) have been designed using solar cell simulator capacitance software (SCAPS-1D, version 3.3.07) to solve the Poisson and continuity equations, and it was created by the Department of Electronics and Information systems, Gent, Belgium [44]. The proposed device architecture is depicted in **Fig. 1**. In these simulations, three different types of CPs-based absorber layers (i.e., $BaZrS_3$ - 1.9 eV, $Ba(Zr_{0.95}Ti_{0.05})S_3$ -1.63 eV, $BaZr(S_{0.6}Se_{0.4})_3$ -1.76 eV), titanium dioxide (TiO_2) as an electron transport layer (ETL), and cuprous oxide (Cu_2O) as a hole transport layer (HTL) were used. All the simulations were carried out under one sun AM 1.5 G (100 $mW.cm^{-2}$) solar spectrum with the working temperature of 300 K and without considering the optical reflectance of each layer at the interface nor surface.

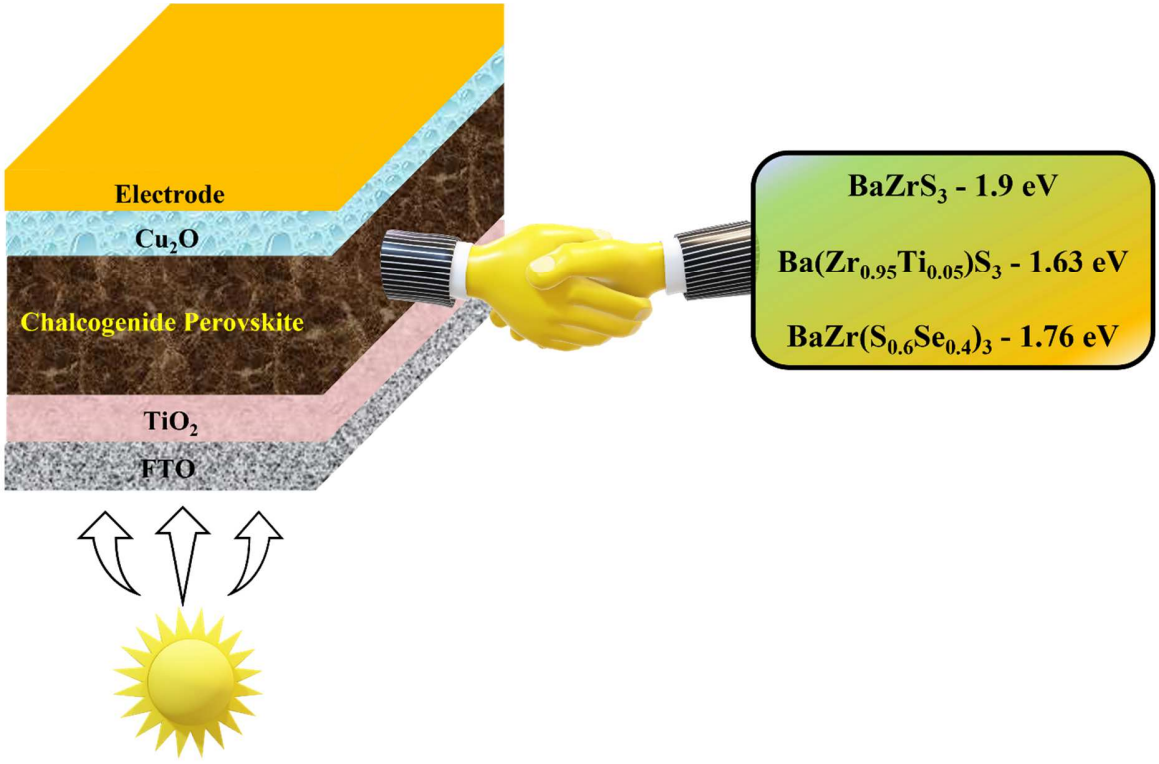

Fig. 1. The n-i-p typical CPs solar cell structure.

In the initial stage, the parasitic resistances (i.e., R_{Series} and R_{Shunt}) are not considered, but the effect of parasitic resistances and the working temperature are explored at the end of this paper.

The traditional SCAPS optical absorption model with square root submodel (i.e., $\alpha(h\upsilon) = \alpha_0+\beta_0(Eg/h\upsilon))((h\upsilon/Eg)-1)^{1/2}$) was used to obtain the absorption coefficients of the various layers (i.e. ETL, CPs absorber, HTL). All layers input parameters such as optical band-gap, electron (e^-) and hole (h^+) mobility, e^- affinity and all other details are taken from previously published experimental and theoretical results, listed in **Table 1**, and the adopted ETL/CPs and CPs/HTL interface defect parameters shown in **Table 2** [4,5,13,26,45,46]. The employed e^- and h^+ thermal velocity values are considered as 1×10^7 cm.s^{-1}, and the work function of front contact (i.e., FTO) and back contact (i.e., Au) are set to 4.4 eV and 5.1 eV, respectively.

Table 1. Initial input parameters for all layers (i.e., FTO, ETL, CPs absorbers, HTL) used in the proposed device model.

	FTO (TCO)	**TiO_2 (ETL)**	**$BaZrS_3$ (Absorber)**	**$Ba(Zr_{0.95}Ti_{0.05})S_3$ (Absorber)**	**$BaZr(S_{0.6}Se_{0.4})_3$ (Absorber)**	**Cu_2O (HTL)**
Thickness (nm)	500	30	500	500	500	100
Bandgap (eV)	3.50	3.20	1.9	1.63	1.76	2.17
Affinity	4.00	3.9	4.10	4.10	4.10	3.2
Permittivity	9.00	9.00	9.6	9.6	9.6	7.11
Effective density of states at CB	2.2×10^{18}	2.2×10^{18}	2.2×10^{18}	2.2×10^{18}	2.2×10^{18}	2.02×10^{17}
Effective density of states at VB	1.8×10^{19}	1.8×10^{19}	1.8×10^{19}	1.8×10^{19}	1.8×10^{19}	1.1×10^{19}
Mobility of electrons	20	20	0.017	0.017	0.017	200
Mobility of holes	10	10	0.059	0.059	0.059	80
Density of n-type doping	1.0×10^{18}	1.0×10^{19}	1.0×10^{12}	1.0×10^{12}	1.0×10^{12}	0
Density of p-type doping	0	1	1.0×10^{12}	1.0×10^{12}	1.0×10^{12}	1.0×10^{18}
Density of defects	1.0×10^{15}	1.0×10^{15}	1.0×10^{15}	1.0×10^{15}	1.0×10^{15}	1.0×10^{15}
Reference	[47]	[45]		[5][4][13]		[46]

Table 2. Interface defects (i.e., ETL/CPs and CPs/HTL) employed in the simulated model.

Parameters	**ETL/CPs**	**CPs/HTL**
Defect type	neutral	neutral
Capture cross-section e^-'s (cm^2)	1.0×10^{-15}	1.0×10^{-18}
Capture cross-section h^+'s (cm^2)	1.0×10^{-15}	1.0×10^{-16}
Energetic distribution	Single	Single
Reference for defect energy level (E_t)	Above the highest Ev	Above the highest Ev
Energy with respect to reference (eV)	0.600	0.050
Total defect ($1/cm^2$)	1.0×10^{11}	1.0×10^{12}

3. Result and discussion

In general, the absorption coefficient of a semiconducting material plays a prominent role in determining device performance. The plot of variations of the absorption coefficient for the ETL, CPs absorbers, and HTL layers using the traditional SCAPS optical absorption model shows the variation as a photon energy function, shown in **Fig. 2**. SCAPS software-generated absorption coefficient (α) of all three CPs absorbers (i.e., $BaZrS_3$, $Ba(Zr_{0.95}Ti_{0.05})S_3$ and $BaZr(S_{0.6}Se_{0.4})_3$) show high values in the band-edge region (>10^5 cm^{-1}), and this confirms the strong light absorption which agrees with the previously published experimental and theoretical results [4,5,8,9,11]. The initial stage of this simulation, FTO (500 nm)/TiO_2 (30 nm)/CPs (i.e., $BaZrS_3$, $Ba(Zr_{0.95}Ti_{0.05})S_3$, $BaZr(S_{0.6}Se_{0.4})_3$ - 500 nm)/Cu_2O (100 nm)/Au device performances are investigated and presented. **Fig. 3a** displays the current-voltage characteristics (J-V) of the three ideal CPs devices from which the main photovoltaic parameters (i.e., short-circuit density - Jsc, fill factor - FF, open-circuit voltage - Voc and PCE) are extracted, and these values are summarized and presented in **Table 3**. The first level of simulation shows that the $Ba(Zr_{0.95}Ti_{0.05})S_3$ chalcogenide perovskite absorber-based device provides higher efficiency than other devices due to the variation of optical band-gaps. As a consequence, a significant decrease is observed in the current density value from 19.1 mA/cm^2 down to 15.8 mA/cm^2 and 12.1 mA/cm^2 for $BaZr(S_{0.6}Se_{0.4})_3$ and, $BaZrS_3$ devices, respectively. The obtained quantum efficiency (QE) graphs for all three devices are displayed in **Fig. 3b**. Due to different absorber layer band-gaps, optical absorption edge shifts from 660 nm (i.e., $BaZrS_3$) to 710 nm and 770 nm for $BaZr(S_{0.6}Se_{0.4})_3$ and $Ba(Zr_{0.95}Ti_{0.05})S_3$ and the simulated QE curves almost cover the complete visible spectrum (see **Fig. 3b**), respectively.

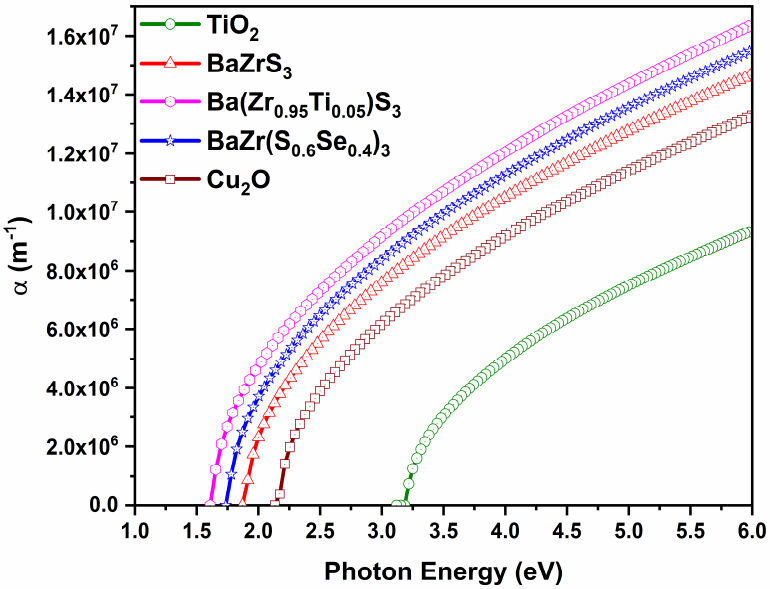

Fig. 2. The absorption coefficient of ETL, CPs absorbers, and HTL layers.

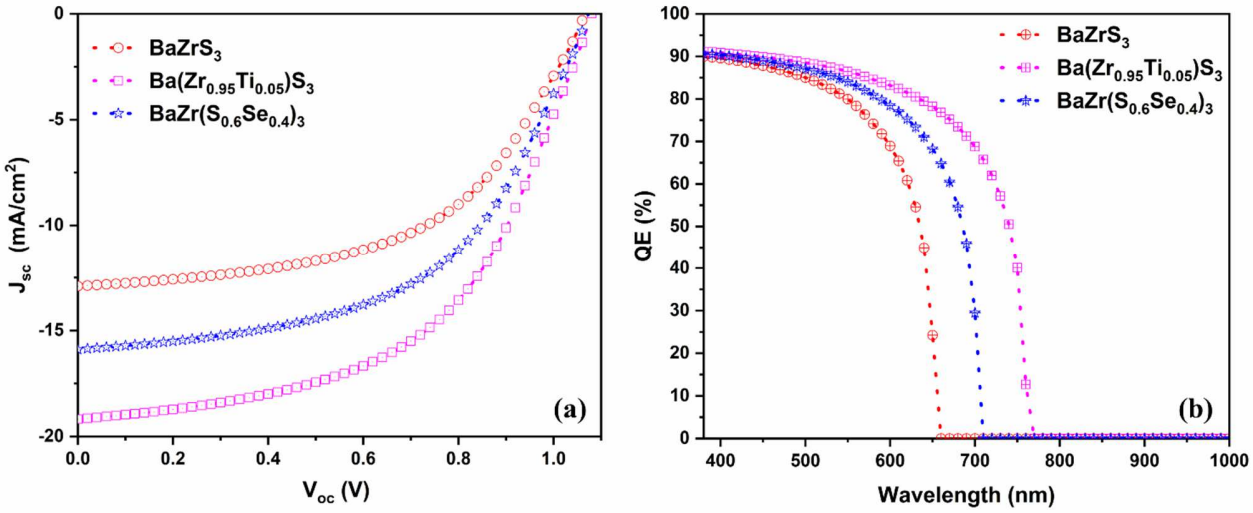

Fig. 3. Current density- voltage (J-V) characteristic (a) and Quantum efficiency (QE) curves (b) of n-i-p CPs devices.

Table 3. Summarized photovoltaic parameters of simulated ideal CPs devices.

Device (500 nm)	J_{sc} (mA/cm^2)	FF (%)	V_{oc} (V)	PCE (%)
$BaZrS_3$	12.90	53.30	1.06	7.33
$Ba(Zr_{0.95}Ti_{0.05})S_3$	19.18	53.13	1.08	11.01
$BaZr(S_{0.6}Se_{0.4})_3$	15.89	53.22	1.07	9.08

3.1 Effect of CPs absorber layer thickness

In general, the absorber layer thickness can greatly influence device performance. It is well-known that increasing the absorber thickness generally leads to more photons absorption (i.e., more charge carrier generation), while thicker layers can be detrimental to charge extraction if charge diffusion lengths are limited. In this section, we have varied the CPs absorber thickness range from 100 nm to 600 nm to understand the effect and find the optimal thickness value to enhance the device efficiency. The obtained device PV performance parameters are demonstrated in **Fig. 4**, and it reveals that the device PCE significantly improves from 6.4% to 8.2% for $BaZrS_3$ device, 9.6% to 12.4% for $Ba(Zr_{0.95}Ti_{0.05})S_3$ model, and 7.9% to 10.2% for $BaZr(S_{0.6}Se_{0.4})_3$ device while increasing the absorber layer thickness from 100 to 300 nm. After that, it continuously decreases due to a CPs layer thickness beyond the optimal limit and more than the charge carrier diffusion length can possibly create higher recombination within the layer. Such limitation is therefore intrinsically associated with the defect/trap density, which we consider in the next section.

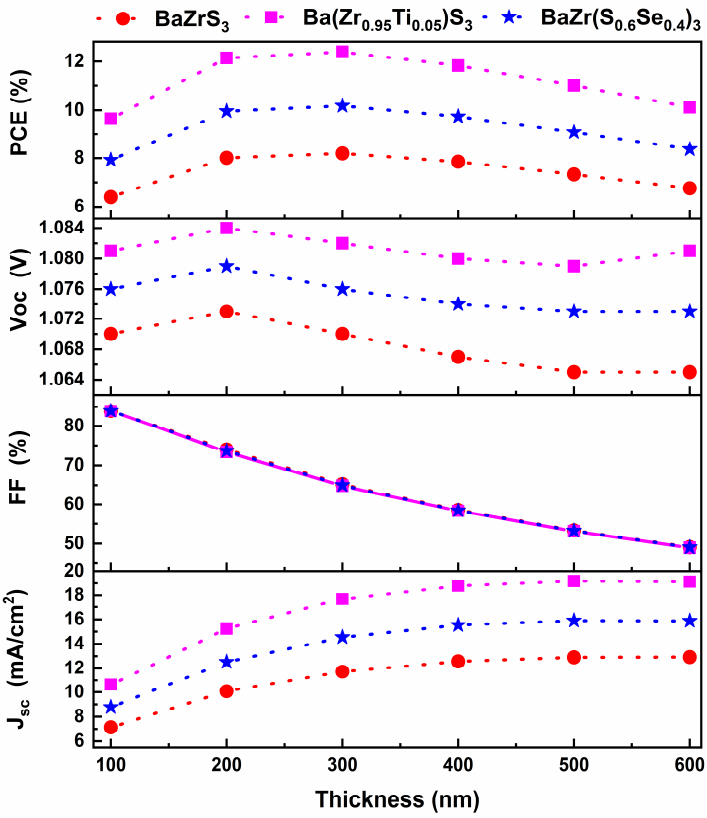

Fig. 4. Change in device PV parameters against absorber layer thickness variation.

3.2 Effect of CPs absorber defect density

The absorber's defect density is also essential to the device's performance, which directly depends on the perovskite layer quality. Experimentally, in PSCs, the defects are located at the surface or interface and/or grain boundaries due to the dangling bonds, uncoordinated atoms, surface dislocation on the film surface, and the lack of stoichiometric compositions at the surfaces of grains and the sublimation of organic molecules during the thermal annealing process, etc. [48]. Also, bulk defects such as intrinsic point defects (i.e., vacancy and interstitial defects), Schottky and Frenkel defects greatly influence the perovskite properties [49,50]. In case of an absorber layer of poor quality, a large number of charge carriers might be lost during the collection of photo-generated charge carriers, which therefore alter device performance. In general, the higher defect density affects charge carrier lifetime and diffusion length, which produces higher recombination issues [51,52]. Therefore, in this section, the impact of CPs absorber defect density (N_t) over the device PV parameters were systematically investigated while varying the values from 10^{10} cm^{-3} to 10^{16} cm^{-3}, shown in **Fig. 5**.

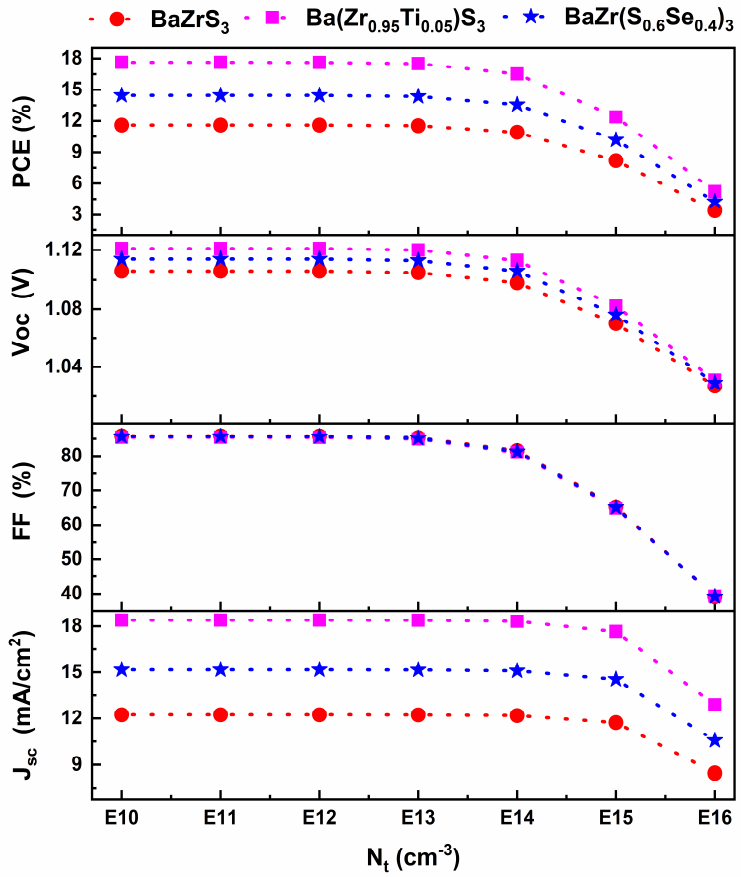

Fig. 5. Variation of device PV parameters with respect to the CPs absorber defect density.

It is found that the device PCE is not shifting a lot while varying N_t values from 10^{10} cm^{-3} to 10^{13} cm^{-3} (i.e., ~ 18% for $Ba(Zr_{0.95}Ti_{0.05})S_3$ device, ~15% for $BaZr(S_{0.6}Se_{0.4})_3$ device, and ~ 12% for $BaZrS_3$ device). Then, it gradually decreased below 5% for all three cases, which is possibly attributed to a higher number of recombinations. On the other hand, we did not observe any significant changes in FF and Voc values (**Fig. 5**) until N_t increased above 10^{13} cm^{-3}. Diffusion lengths of electrons and holes get possibly reduced while increasing absorber defect density value [53]. Therefore, lower N_t values provide excellent device performance due to less recombination rate inside the CPs layer [27]. In the following section, we will use the optimised and chosen value of $N_t = 10^{11}$ cm^{-3} for all three devices and vary the ETL/CPs, and CPs/HTL interface defect densities to understand the effect over the device PV parameters.

3.3 Effect of ETL/CPs and CPs/HTL interface defect density

In general, interfacial defects (i.e., charge recombination centers) are created in the PSCs because of the structural mismatch between two materials or by the introduction of impurities associated with the environment. The impact of the processing technique used (especially from solution) is also crucial in the field of third-generation solar cells. Also, non-radiative losses occur due to the imperfections within the perovskite absorber and the inadequate electronic quality of

perovskite/charge extraction layer heterojunctions, which induce the Voc loss [54]. Therefore, in this section, two interfacial contacts such as TiO_2/CPs and CPs/Cu_2O are considered to investigate the interfacial defects over the device performance. At the TiO_2/CPs, the density of interface defect states is varied from 10^9 cm^{-3} to 10^{15} cm^{-3} with a defect state localized above of the valence band edge (Ev).

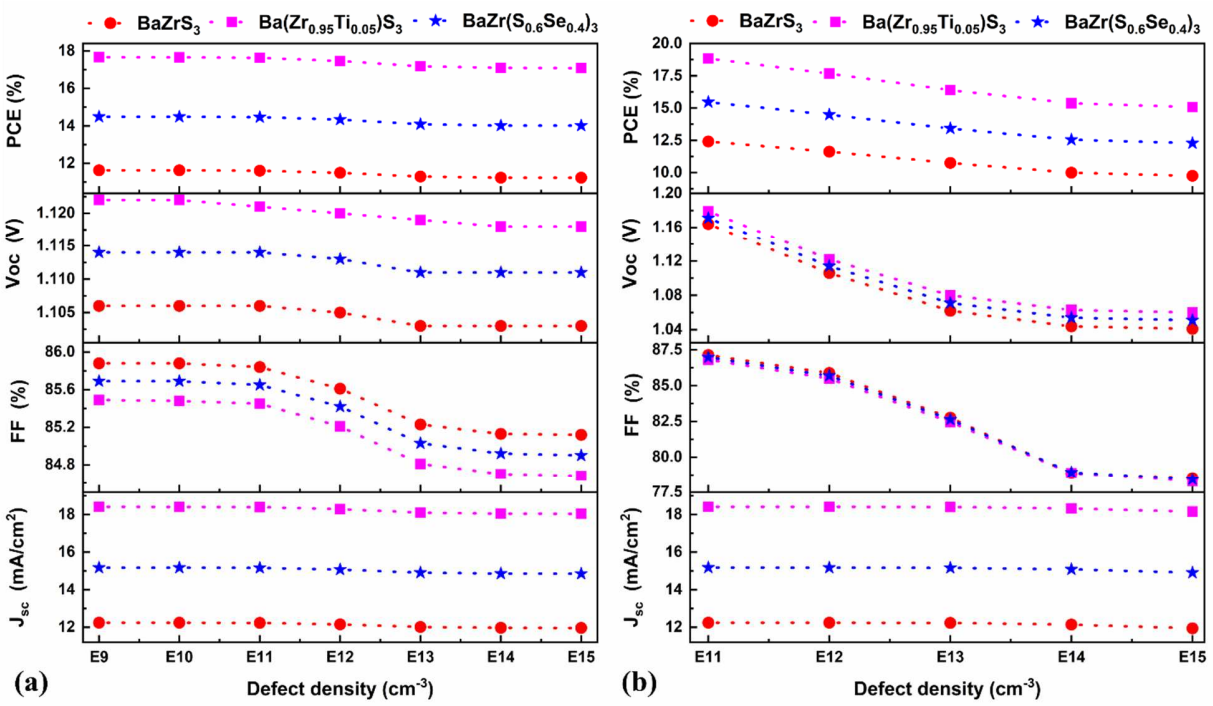

Fig. 6. Variation of device PV parameters as a function of defect density at (a) TiO_2/CPs interface (b) CPs/Cu_2O interface.

Fig. 6a shows the effect of this defect density at the TiO_2/CPs interface on PV performance. We find that the FF and V_{oc} of all three devices reduce drastically for a density above 10^{11} cm^{-3}. On the other hand, from 10^{11} cm^{-3} to 10^{15} cm^{-3}, Jsc also significantly decreased for all devices. These reductions in device performance is directly due to trap-assisted recombination associated with this interface [55]. We note that once the minimal amount of defect is reached to ensure good device performance, further reduction in the TiO_2/CPs defect density does not bring additional benefit.

Similarly, the defect density at the CPs/Cu_2O interface was varied from 10^{11} cm^{-3} to 10^{15} cm^{-3} without changing other input parameters, as depicted in **Fig. 6b**. This defect density alters drastically the PCE of the devices, which decreases from 12.42% to 9.76% for $BaZrS_3$, 18.85% to 15.08% for $Ba(Zr_{0.95}Ti_{0.05})S_3$ and 15.47% to 12.29% for $BaZr(S_{0.6}Se_{0.4})_3$ devices, respectively. Also, we noticed that the FF and Voc of all three devices were reduced for a defect density above 10^{11} cm^{-3}. Hence, it is clear that the ETL/perovskite interface plays a less dominant role than the perovskite/HTL interface [56,57]. It might be related to a higher charge carrier recombination due

to a larger defect density (i.e., more defects) in the perovskite/HTL interface. After testing the different defect density values, even below 10^{11} cm^{-3}, the simulated device model is already close to the optimal performance, and a further reduction in defect density is not crucial. Therefore, it is clear that increments in both TiO_2/CPs and CPs/Cu_2O interface defect densities mainly influence the Voc and FF rather than Jsc, which degrade device performance due to more traps and recombination centres. Hence, our simulation indicates that the optimal defect densities for TiO_2/CPs and CPs/Cu_2O interfaces are 10^9 cm^{-3} and 10^{11} cm^{-3}, respectively. After these limits, the PCE of CPs solar cells deteriorates to a significant extent.

In the actual solar cell, the lattice mismatch and surface roughness present at the interfaces creates the interfacial defects, which act as recombination centres for charge carriers. This consideration is essential while fabricating an actual device that causes epitaxial strain, which would influence the epitaxial layer properties and disturb the symmetry at the interfaces (i.e., ETL/absorber and absorber/HTL interface) will generate dislocations, inhomogeneities and defect centers, etc. Therefore, the degrading surface properties of the ETL, absorber or HTL layer drastically influence the device's PV performance [58,59]. Moreover, the lattice constants of the absorber, ETL and HTL layers need to be matched to reduce or suppress the interfacial defects. The following equation is used to calculate the lattice mismatch (δ) based on lattice-constant values for ETL/absorber and absorber/HTL interface [60–62],

$$\delta = \frac{2|a_s - a_e|}{(a_s + a_e)} \qquad (1)$$

Where a_s is the lattice constant of the substrate and a_e is the lattice constant of the epitaxial layer.

Table 4. Lattice mismatch for different CP Absorbers with ETL and HTL.

Layers	Lattice parameters (Å)			Ref	Lattice Mismatch (%)	
					ETL/Absorber	Absorber/HTL
	a	b	c			
$BaZrS_3$	7.061	9.979	7.024	[5]	2.2	49.2
$Ba(Zr_{0.95}Ti_{0.05})S_3$	7.047	9.965	7.018	[5]	2.0	49.0
$BaZr(S_{0.6}Se_{0.4})_3$	7.127	10.066	7.087	[5]	3.1	50.1
TiO_2 (ETL)	3.66	3.66	9.76	[60]		
Cu_2O (HTL)	4.27	-	-	[61]		

Table 4 compares lattice mismatch for different CP absorbers with ETL and HTL. A low lattice mismatch of 2% and 49% values are estimated for the ETL/$Ba(Zr_{0.95}Ti_{0.05})S_3$ and $Ba(Zr_{0.95}Ti_{0.05})S_3$/$Cu_2O$ interfaces. On the other hand, a little higher lattice mismatch values are obtained for the other CPs absorber interfaces with ETL and HTL than the previous one. Therefore, the reduced carrier recombination loss and dislocation or defects at the $Ba(Zr_{0.95}Ti_{0.05})S_3$ CPs interfaces (i.e., with ETL and HTL) may occur due to the relatively low lattice mismatch compared to $BaZrS_3$ and $BaZr(S_{0.6}Se_{0.4})_3$ CPs interfaces. This obtained

mismatch reduction is undoubtedly related to the small Ti concentration at the Zr site, which is more effective than Se substitution at the S site.

After optimizing all the basic input parameters, especially for CPs layers, such as thicknesses, total defect densities (N_t), TiO_2/CPs and CPs/Cu_2O interface defect densities, all these values are collected and repeated in the device simulation using these optimum values. It is worth mentioning here that the ETL (i.e., 30 nm to 100 nm) and HTL (i.e., 100 nm to 150 nm) thicknesses were also tuned to identify the optimum thickness range that enhances the PV parameters (not shown here). No significant effects of these ETL and HTL layers were observed, and we therefore keep the same thickness values for ETL and HTL. The obtained current-voltage characteristics (J-V) and quantum efficiencies of all three optimized CPs devices are depicted in **Fig. 7**. The optimized PV parameters (i.e., Jsc, Voc, FF and PCE) are extracted and presented in **Table 5**.

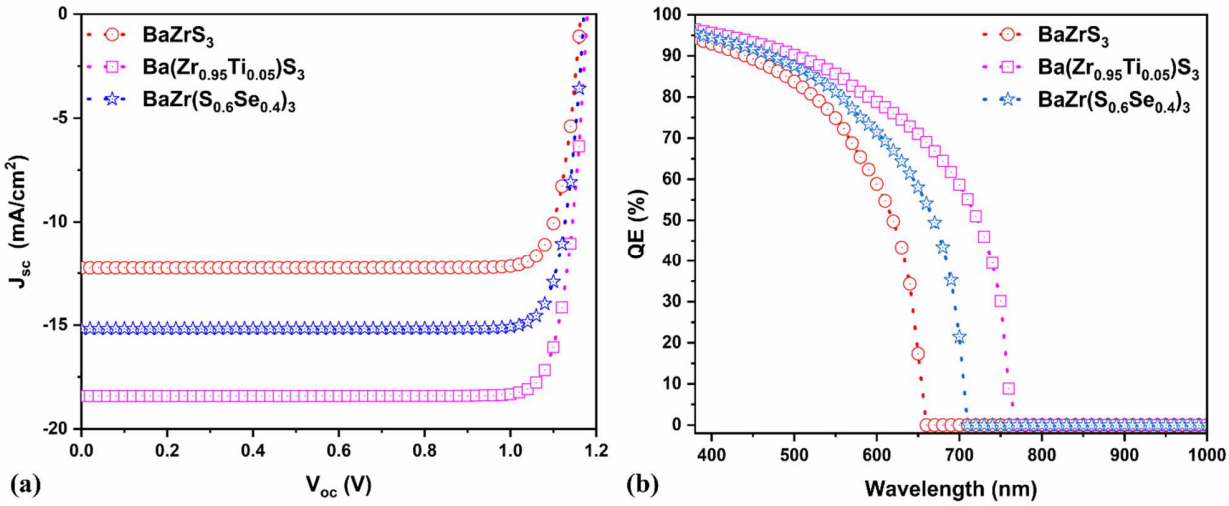

Fig. 7. Current density- voltage characteristic (a) and QE (b) curves of optimized n-i-p CPs devices.

Table 5. Summarized photovoltaic parameters of optimized CPs devices.

Device	J_{sc} (mA/cm^2)	FF (%)	V_{oc} (V)	PCE (%)
$BaZrS_3$	12.24	87.13	1.16	12.42
$Ba(Zr_{0.95}Ti_{0.05})S_3$	18.42	86.81	1.18	18.85
$BaZr(S_{0.6}Se_{0.4})_3$	15.18	86.98	1.17	15.47

The CPs device performances are highly enhanced compared to the initial stage simulation results, for example, PCE from 7.33% to 12.42% for $BaZrS_3$, 11.01% to 18.85% for $Ba(Zr_{0.95}Ti_{0.05})S_3$ and 9.08% to 15.47% for $BaZr(S_{0.6}Se_{0.4})_3$ devices, respectively. (see **Table 3 and Table 5**). The obtained QE graphs (**Fig. 7b**) also shows that the there is a significant improvement occurs in the QE efficiency (<95%) than the initial results. (see **Fig. 3b and Fig.**

7b) All the optimized results clearly show that the CPs absorber thickness, total defect densities, TiO_2/CPs and CPs/Cu_2O interface defect densities play a crucial role in the PV performance enhancement. Especially due to more photons absorption, Ti incorporated $BaZrS_3$ absorber layer (i.e., 1.63 eV) based device showing higher performance than other devices.

3.4 Effect of Parasitic resistances

In real solar cells, both series resistance (R_{Series}) and shunt resistance (R_{Shunt}) (i.e., parasitic resistances) have a massive impact on device PV performance as they govern the shape and slopes of the J–V characteristics [26]. They indeed reflect the main loss mechanisms occurring in the device, and help giving a relevant diagnostic of solar cell operation. In general, high-efficiency devices should have low R_{Series} and higher R_{Shunt} values. R_{shunt} should be reduced compared to the ideal case due to the impact of morphologies of layers (eventual pinholes) or due to leakage currents which can not be avoided in some extent in a real device. Similarly, R_{series} should be tested because, in reality, it depends on the contacts between charge transfer layers (i.e., ETL and HTL) to metal contact layer (i.e., electrical ohmic contact). Sometimes, the migrated ions from the perovskite layer react with the selective contacts and the electrode diffusion to the HTL layer, restricting the charge transfer [63,64]. Therefore, in this section, we explore the impact of a variation of R_{Series} from 1 $\Omega.cm^2$ to 10 $\Omega.cm^{2,}$ and of R_{Shunt} from 1000 $\Omega.cm^2$ to 10000 $\Omega.cm^2$ to better understand how parasitic resistances will affect the behavior of devices optimized in the previous section. The corresponding evolutions of the main photovoltaic parameters are shown in **Fig. 8a and 8b**.

Our simulated results clearly show that a small increment in R_{Series} by a few Ohms already strongly reduces the FF, from 86% to 77% for $BaZrS_3$, 85% to 72% for $Ba(Zr_{0.95}Ti_{0.05})S_3$ and 86% to 75% for $BaZr(S_{0.6}Se_{0.4})_3$ devices, respectively. (see **Fig. 8a**) Therefore, the overall PCE rapidly decreased for all three devices. **Fig. 8b** clearly demonstrates the impact of R_{Shunt} over the CPs performance; increasing R_{Shunt} leads to a rapid increase in FF and PCE values, while Jsc and Voc are only slightly affected by R_{Shunt}. The PCE enhancing from 11.34% to 12.31% for $BaZrS_3$, 17.75% to 18.74% for $Ba(Zr_{0.95}Ti_{0.05})S_3$ and 14.38% to 15.36% for $BaZr(S_{0.6}Se_{0.4})_3$ devices, respectively. Therefore, with the higher values of R_{Shunt}, the device provides improved performance. In a real device, the following strategies are used so far to increase or maintain a minimum value of R_{shunt} to keep the high device performance, (1) solvents additives to enhance the morphology behavior (i.e., to avoid pinholes or voids), (2) using blocking/interface layer or by passivation materials that efficiently block shunt pathways [65–68].

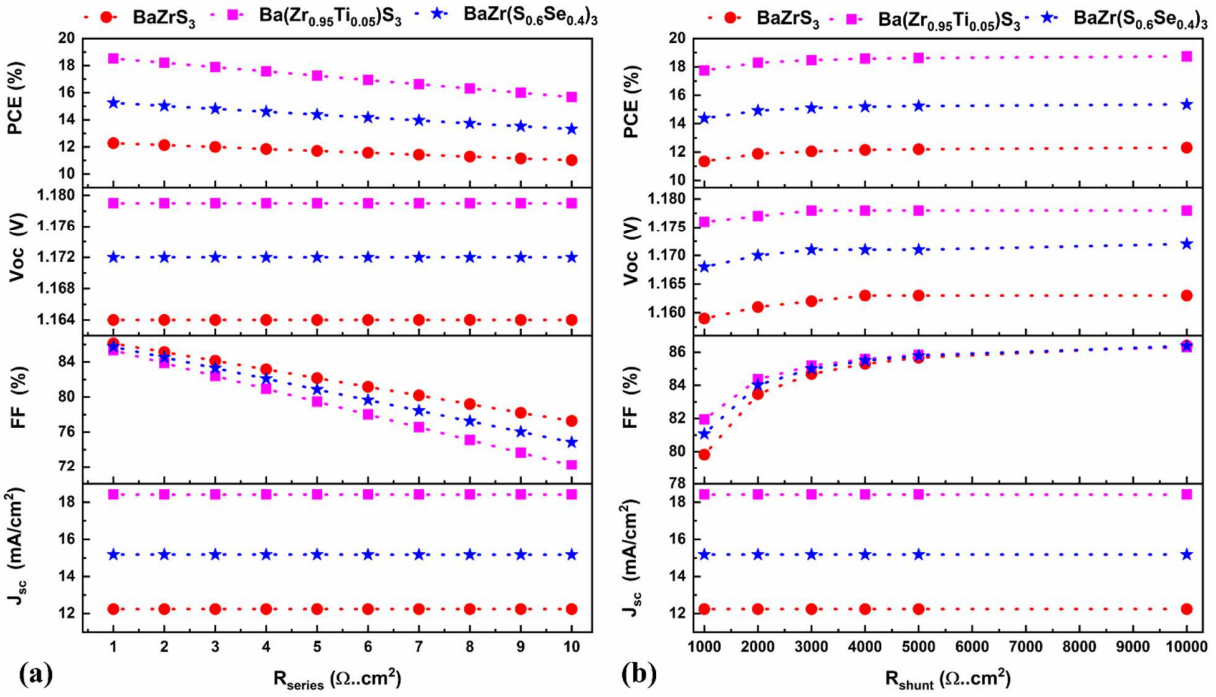

Fig. 8. Variation of device PV parameters as a function of parasitic resistances, Rseries (a), and Rshunt (b).

3.5 Effect of Working temperature

The ambient conditions in the environments with PV installations significantly affect these device performances, notably temperatures. Also, the temperature is higher in space; so far, high-efficiency Si or III-V semiconductor-based solar cells are used to generate power in spacecraft/satellites [69,70]. Therefore, excellent PV device performance is necessary while having a higher temperature, whether down or in space. The perovskite scientific communities are currently showing interest in expanding the PSCs in space application [71–73]. For example, Z. Dong *et al.* fabricated and investigated the PSCs under higher operating temperatures (i.e., 25 - 220°C) to expand the PSCs usage [74]. Therefore, in this section, we study the influence of temperature on device operation, by carrying out simulations between the ambient temperature (300K) up to 400 K (120°C) under a constant illumination of 1 Sun (i.e., 100 mW.cm^{-2}, AM1.5G standard spectrum without changing any other simulation parameters. The corresponding temperature-dependent PV parameters are shown in **Fig. 9.**

Increasing the temperature values resulted in a considerable reduction in all PV parameters (excluding Jsc), especially the FF and Voc values. The Voc behavior and dependence on temperature described by the relation [53,75];

$$\frac{d(V_{OC})}{dT} = \frac{V_{OC}}{T} - \frac{{}^{E_q}/_{q}}{T} \qquad (2)$$

The decrease in the Voc values associated with increasing temperatures (Eqn. 2) enhances the reverse saturation current. The reduction in Voc with increasing temperature (**Fig. 9**) results in a clear decrease of the power conversion efficiency. Also, the increasing temperature may lead to the electrons' thermal excitation, causing some vibrations and eventual instability, which leads to recombinations of the charge carriers [76].

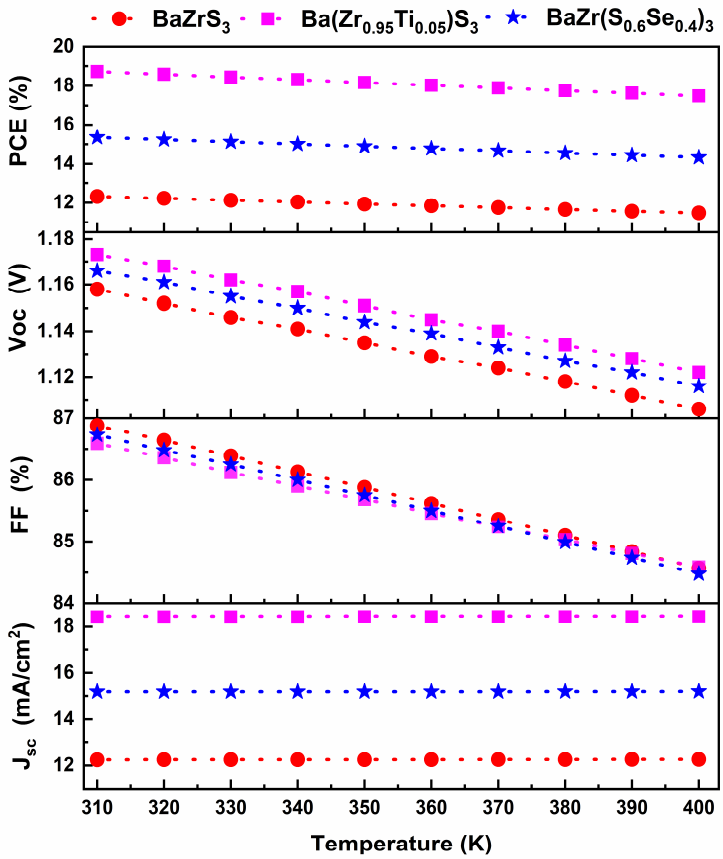

Fig. 9. Variation of device PV parameters as a function of different working temperatures.

Table 6 summarises the photovoltaic performance comparison between predicted maximum PCE using SLME and Double-reflection model (DRM) with the current SCAPS simulation results. Usually, the SLME model is based on photons absorption limited by the thickness of absorbers, which is crucial (i.e., optical transition types and absorption spectra) for any photovoltaic materials to find the potential absorbers [77,78]. According to previous reports using the SLME and DRM, it has been demonstrated that CPs, especially $BaZrS_3$, $Ba(Zr_{0.95}Ti_{0.05})S_3$, and $BaZr(S_{0.6}Se_{0.4})_3$ are interesting materials for photovoltaic applications either in single or multi-junction solar cells [4,5,12]. It is clearly evident from this simulation and previous results the appropriate amount of Ti incorporated $BaZrS_3$ devices deliver higher efficiency than Se doped single and tandem models (see **Table 6**). Besides, Ti is an earth-abundant and non-toxic element that is highly beneficial in order to produce environmentally friendly photovoltaic devices [5]. Additionally, experimental observation shows that band-edge absorption broadening occurs while

adding Ti (Zr site) or Se (S site), which significantly increase the Urbach energy (for example, 28.1 meV for $BaZrS_3$, 49.6 meV for $BaZr(S_{0.6}Se_{0.4})_3$ and 70.8 meV for $Ba(Zr_{0.95}Ti_{0.05})S_3$) [5]. S. Nazerdeylami's results propose that the bimolecular recombination rate decreases while increasing Urbach energy [79] which might be another reason for the enhanced efficiency for $Ba(Zr_{0.95}Ti_{0.05})S_3$ device. As a result, further insightful experimental (actual) device fabrication and results are essential to understand more device physics for these kinds of chalcogenide perovskites absorbers based solar cells.

Table 6. Photovoltaic performance comparison between predicted maximum PCE with the current simulation result.

Device (Absorbers)	E_g (eV)	Thickness (nm)	PCE (%)	Ref
$BaZrS_3$	1.70	300	22.00	
$BaZrSeS_2$	1.48	300	24.00	SLME
$BaZrSe_3$	1.35	300	27.00	calculated
$Ba(Zr_{0.5}Ti_{0.5})S_3$	1.00	300	29.00	Max. PCE's [4]
$Ba(Zr_{0.75}Ti_{0.25})S_3$	1.10	300	28.00	
$BaZrS_3$	1.87	1000	25.02	SLME
$CaZrS_3$	2.04	1000	21.33	calculated
α-$SrZrS_3$	1.40	1000	25.45	Max. PCE's [12]
β-$SrZrS_3$	2.05	1000	21.19	
Sr_2SbTaS_6	1.02	300	22.28	
Sr_2BiNbS_6	1.38	300	17.39	
Sr_2BiTaS_6	1.46	300	16.31	SLME
Ba_2SbTaS_6	1.26	300	20.77	calculated
Ba_2BiNbS_6	1.51	300	14.92	Max. PCE's [80]
Ba_2BiTaS_6	1.56	300	14.32	
Ba_2SbTaS_6	1.21	300	24.04	
Ba_2BiNbS_6	1.69	300	20.75	
$Ba_2BiTaSe_6$	1.11	300	27.63	
$BaHf_{1-x}Zr_xS_3$ (X=0.00)	1.34	500	22.45	
X=0.25	1.26	500	25.94	SLME
X=0.50	1.20	500	28.99	calculated
X=0.75	1.19	500	29.40	Max. PCE's [81]
X=1.00	1.08	500	30.45	
$BaZrS_3$ (Top cell)/c-Si tandem	1.94	**Top cell**	29.00	DRM
$Ba(Zr_{0.95}Ti_{0.05})S_3$ (Top cell)/c-Si tandem	1.63	**thickness**	35.00	calculated
$BaZr(S_{0.6}Se_{0.4})_3$ (Top cell)/c-Si tandem	1.76	300	32.50	PCE's [5]
$BaZrS_3$	1.90	300	12.42	SCAPS simulation
$Ba(Zr_{0.95}Ti_{0.05})S_3$	1.63	300	18.85	results

$BaZr(S_{0.6}Se_{0.4})_3$	1.76	300	15.47	[This work]

4. Conclusion

In this work, $BaZrS_3$, $Ba(Zr_{0.95}Ti_{0.05})S_3$ and $BaZr(S_{0.6}Se_{0.4})_3$ Chalcogenide perovskite absorber layers-based n-i-p solar cells were systematically modeled and simulated using SCAPS-1D. The final device performance improved from 7.33% to 12.42% for $BaZrS_3$, 11.01% to 18.85% for $Ba(Zr_{0.95}Ti_{0.05})S_3$ and 9.08% to 15.47% for $BaZr(S_{0.6}Se_{0.4})_3$ devices for optimized layer thicknesses, and optimized total and interfacial defect densities. These results indicate that $Ba(Zr_{0.95}Ti_{0.05})S_3$ CPs absorber is a promising candidate for high-efficiency solar cells, compared to the other compounds tested here. Our simulation studies show the effects of parasitic resistances (R_{Series} and R_{Shunt}) and working temperature. These simulation findings are helpful for further understanding of the chalcogenide perovskites single-junction devices.

CRediT authorship contribution statement

S. Karthick: Writing – original draft, contributed to the simulation, analyzed the results, review & editing. **S. Velumani and J. Bouclé**: Review & editing, validation. All authors have given significant feedback and approved the final version.

References

[1] Best Research-Cell Efficiency Chart | Photovoltaic Research | NREL, (n.d.). https://www.nrel.gov/pv/cell-efficiency.html (accessed November 7, 2021).

[2] D. Tiwari, O.S. Hutter, G. Longo, Chalcogenide perovskites for photovoltaics: current status and prospects, J. Phys. Energy. 3 (2021) 034010. https://doi.org/10.1088/2515-7655/ABF41C.

[3] Q.A. Akkerman, L. Manna, What Defines a Halide Perovskite?, ACS Energy Lett. (2020) 604–610. https://doi.org/10.1021/ACSENERGYLETT.0C00039.

[4] W. Meng, B. Saparov, F. Hong, J. Wang, D.B. Mitzi, Y. Yan, Alloying and Defect Control within Chalcogenide Perovskites for Optimized Photovoltaic Application, Chem. Mater. 28 (2016) 821–829. https://doi.org/10.1021/ACS.CHEMMATER.5B04213.

[5] Y. Nishigaki, T. Nagai, M. Nishiwaki, T. Aizawa, M. Kozawa, K. Hanzawa, Y. Kato, H. Sai, H. Hiramatsu, H. Hosono, H. Fujiwara, Extraordinary Strong Band-Edge Absorption in Distorted Chalcogenide Perovskites, Sol. RRL. 4 (2020) 1900555. https://doi.org/10.1002/SOLR.201900555.

[6] Y.-Y. Sun, M.L. Agiorgousis, P. Zhang, S. Zhang, Chalcogenide Perovskites for Photovoltaics, Nano Lett. 15 (2015) 581–585. https://doi.org/10.1021/NL504046X.

[7] C. Comparotto, A. Davydova, T. Ericson, L. Riekehr, M. V. Moro, T. Kubart, J. Scragg, Chalcogenide Perovskite BaZrS3: Thin Film Growth by Sputtering and Rapid Thermal Processing, ACS Appl. Energy Mater. 3 (2020) 2762–2770. https://doi.org/10.1021/ACSAEM.9B02428.

[8] J.A. Márquez, M. Rusu, H. Hempel, I.Y. Ahmet, M. Kölbach, I. Simsek, L. Choubrac, G.

Gurieva, R. Gunder, S. Schorr, T. Unold, BaZrS3 Chalcogenide Perovskite Thin Films by H2S Sulfurization of Oxide Precursors, J. Phys. Chem. Lett. 12 (2021) 2148–2153. https://doi.org/10.1021/ACS.JPCLETT.1C00177.

[9] X. Wei, H. Hui, C. Zhao, C. Deng, M. Han, Z. Yu, A. Sheng, P. Roy, A. Chen, J. Lin, D.F. Watson, Y.Y. Sun, T. Thomay, S. Yang, Q. Jia, S. Zhang, H. Zeng, Realization of BaZrS3 chalcogenide perovskite thin films for optoelectronics, Nano Energy. 68 (2020) 104317. https://doi.org/10.1016/J.NANOEN.2019.104317.

[10] Z. Yu, X. Wei, Y. Zheng, H. Hui, M. Bian, S. Dhole, J.H. Seo, Y.Y. Sun, Q. Jia, S. Zhang, S. Yang, H. Zeng, Chalcogenide perovskite BaZrS3 thin-film electronic and optoelectronic devices by low temperature processing, Nano Energy. 85 (2021) 105959. https://doi.org/10.1016/J.NANOEN.2021.105959.

[11] S. Sharma, Z. Ward, K. Bhimani, K. Li, A. Lakhnot, R. Jain, S.-F. Shi, H. Terrones, N. Koratkar, Bandgap Tuning in BaZrS3 Perovskite Thin Films, ACS Appl. Electron. Mater. 3 (2021) 3306–3312. https://doi.org/10.1021/ACSAELM.1C00575.

[12] M. Kumar, A. Singh, D. Gill, S. Bhattacharya, Optoelectronic Properties of Chalcogenide Perovskites by Many-Body Perturbation Theory, J. Phys. Chem. Lett. 12 (2021) 5301–5307. https://doi.org/10.1021/ACS.JPCLETT.1C01034/SUPPL_FILE/JZ1C01034_SI_001.PDF.

[13] V.K. Ravi, S.H. Yu, P.K. Rajput, C. Nayak, D. Bhattacharyya, D.S. Chung, A. Nag, Colloidal BaZrS3 chalcogenide perovskite nanocrystals for thin film device fabrication, Nanoscale. 13 (2021) 1616–1623. https://doi.org/10.1039/D0NR08078K.

[14] Mamta, K.K. Maurya, V.N. Singh, Sb2Se3 versus Sb2S3 solar cell: A numerical simulation, Sol. Energy. 228 (2021) 540–549. https://doi.org/10.1016/J.SOLENER.2021.09.080.

[15] V.C. Karade, J.S. Jang, D. Kumbhar, M. Rao, P.S. Pawar, S. Kim, K.S. Gour, J. Park, J. Heo, T.D. Dongale, J.H. Kim, Combating open circuit voltage loss in Sb2Se3 solar cell with an application of SnS as a back surface field layer, Sol. Energy. 233 (2022) 435–445. https://doi.org/10.1016/J.SOLENER.2022.01.010.

[16] I. Gharibshahian, A.A. Orouji, S. Sharbati, Alternative buffer layers in Sb2Se3 thin-film solar cells to reduce open-circuit voltage offset, Sol. Energy. 202 (2020) 294–303. https://doi.org/10.1016/J.SOLENER.2020.03.115.

[17] Mamta, K.K. Maurya, V.N. Singh, Enhancing the Performance of an Sb2Se3-Based Solar Cell by Dual Buffer Layer, Sustain. 2021, Vol. 13, Page 12320. 13 (2021) 12320. https://doi.org/10.3390/SU132112320.

[18] A. Srivastava, T.R. Lenka, S.K. Tripathy, SCAPS-1D Simulations for Comparative Study of Alternative Absorber Materials Cu<Subscript>2</Subscript>XSnS<Subscript>4</Subscript> (<Emphasis Type="Italic">X</Emphasis> = Fe, Mg, Mn, Ni, Sr) in CZTS-Based Solar Cells, Lect. Notes Electr. Eng. 781 (2022) 329–337. https://doi.org/10.1007/978-981-16-3767-4_31.

[19] M.D. Haque, M.H. Ali, A.Z.M.T. Islam, Efficiency enhancement of WSe2 heterojunction

solar cell with CuSCN as a hole transport layer: A numerical simulation approach, Sol. Energy. 230 (2021) 528–537. https://doi.org/10.1016/J.SOLENER.2021.10.054.

[20] M. Minbashi, A. Ghobadi, M.H. Ehsani, H. Rezagholipour Dizaji, N. Memarian, Simulation of high efficiency SnS-based solar cells with SCAPS, Sol. Energy. 176 (2018) 520–525. https://doi.org/10.1016/J.SOLENER.2018.10.058.

[21] X. Zhou, J. Han, Design and simulation of C_2N based solar cell by SCAPS-1D software, Mater. Res. Express. 7 (2020) 126303. https://doi.org/10.1088/2053-1591/abcdd6.

[22] J. Capistrán-Martínez, D. Loeza-Díaz, D. Mora-Herrera, F. Pérez-Rodríguez, M. Pal, Theoretical evaluation of emerging Cd-free Cu3BiS3 based solar cells using experimental data of chemically deposited Cu3BiS3 thin films, J. Alloys Compd. 867 (2021) 159156. https://doi.org/10.1016/J.JALLCOM.2021.159156.

[23] Y. Meng, B.R. Magruder, H.W. Hillhouse, On interface recombination, series resistance, and absorber diffusion length in BiI3 solar cells, J. Appl. Phys. 129 (2021) 133101. https://doi.org/10.1063/5.0034776.

[24] B. Sharma, A.S. Mathur, V.K. Rajput, I.K. Singh, B.P. Singh, Device modeling of non-fullerene organic solar cell by incorporating CuSCN as a hole transport layer using SCAPS, Optik (Stuttg). 251 (2022) 168457. https://doi.org/10.1016/J.IJLEO.2021.168457.

[25] M. Kumar, A. Raj, A. Kumar, A. Anshul, Effect of band-gap tuning on lead-free double perovskite heterostructure devices for photovoltaic applications via SCAPS simulation, Mater. Today Commun. 26 (2021) 101851. https://doi.org/10.1016/J.MTCOMM.2020.101851.

[26] S. Karthick, S. Velumani, J. Bouclé, Experimental and SCAPS simulated formamidinium perovskite solar cells: A comparison of device performance, Sol. Energy. (2020). https://doi.org/10.1016/j.solener.2020.05.041.

[27] S. Abdelaziz, A. Zekry, A. Shaker, M. Abouelatta, Investigating the performance of formamidinium tin-based perovskite solar cell by SCAPS device simulation, Opt. Mater. (Amst). (2020). https://doi.org/10.1016/j.optmat.2020.109738.

[28] I. Mukherjee, S. Somay, S.K. Pandey, Comprehensive Device Modeling and Performance Analysis of Quantum Dot-Perovskite Solar Cells, J. Electron. Mater. (2022) 1–9. https://doi.org/10.1007/S11664-021-09409-2/TABLES/4.

[29] H. mouhib, A.A. Hssi, Y.A. Wahmane, L. Atourki, A. Elfanaoui, A. Ihlal, K. Bouabid, Numerical investigation of eco-friendly MASnI3 perovskite-based solar cell: effect of defect density and hole transport layer, Model. Simul. Mater. Sci. Eng. (2022). https://doi.org/10.1088/1361-651X/AC55B0.

[30] M.A. Shafi, H. Ullah, S. Ullah, L. Khan, S. Bibi, B.M. Soucase, Numerical Simulation of Lead-Free Sn-Based Perovskite Solar Cell by Using SCAPS-1D, in: 1st Int. Conf. Energy, Power Environ., MDPI, Basel Switzerland, 2022: p. 92. https://doi.org/10.3390/engproc2021012092.

[31] D. Jayan K, V. Sebastian, J. Kurian, Simulation and optimization studies on CsPbI3 based inorganic perovskite solar cells, Sol. Energy. 221 (2021) 99–108.

https://doi.org/10.1016/J.SOLENER.2021.04.030.

[32] M. Mehrabian, E.N. Afshar, S.A. Yousefzadeh, Simulating the thickness effect of the graphene oxide layer in CsPbBr3- based solar cells, Mater. Res. Express. 8 (2021) 035509. https://doi.org/10.1088/2053-1591/ABF080.

[33] A. Chauhan, A. Oudhia, A.K. Shrivastav, Analysis of eco-friendly tin-halide Cs2SnI6-based perovskite solar cell with all-inorganic charge selective layers, J. Mater. Sci. Mater. Electron. 33 (2022) 1670–1685. https://doi.org/10.1007/S10854-022-07723-X/FIGURES/14.

[34] M.R. Jani, M.T. Islam, S.M. Al Amin, M.S. Us Sami, K.M. Shorowordi, M.I. Hossain, S. Chowdhury, S.S. Nishat, S. Ahmed, Exploring solar cell performance of inorganic Cs2TiBr6 halide double perovskite: A numerical study, Superlattices Microstruct. 146 (2020) 106652. https://doi.org/10.1016/J.SPMI.2020.106652.

[35] D. Saikia, J. Bera, A. Betal, S. Sahu, Performance evaluation of an all inorganic CsGeI3 based perovskite solar cell by numerical simulation, Opt. Mater. (Amst). 123 (2022) 111839. https://doi.org/10.1016/J.OPTMAT.2021.111839.

[36] A.J. Kale, R. Chaurasiya, A. Dixit, Inorganic Lead-Free Cs2AuBiCl6 Perovskite Absorber and Cu2O Hole Transport Material Based Single-Junction Solar Cells with 22.18% Power Conversion Efficiency, Adv. Theory Simulations. 4 (2021) 2000224. https://doi.org/10.1002/ADTS.202000224.

[37] Y. He, L. Xu, C. Yang, X. Guo, S. Li, K. Lutfi, A. Putri, M. Rahman, V. Keller, Design and Numerical Investigation of a Lead-Free Inorganic Layered Double Perovskite Cs4CuSb2Cl12 Nanocrystal Solar Cell by SCAPS-1D, Nanomater. 2021, Vol. 11, Page 2321. 11 (2021) 2321. https://doi.org/10.3390/NANO11092321.

[38] S.S. Hussain, S. Riaz, G.A. Nowsherwan, K. Jahangir, A. Raza, M.J. Iqbal, I. Sadiq, S.M. Hussain, S. Naseem, Numerical Modeling and Optimization of Lead-Free Hybrid Double Perovskite Solar Cell by Using SCAPS-1D, J. Renew. Energy. 2021 (2021) 1–12. https://doi.org/10.1155/2021/6668687.

[39] D. Stanić, V. Kojić, T. Čižmar, K. Juraić, L. Bagladi, J. Mangalam, T. Rath, A. Gajović, Simulating the Performance of a Formamidinium Based Mixed Cation Lead Halide Perovskite Solar Cell, Mater. 2021, Vol. 14, Page 6341. 14 (2021) 6341. https://doi.org/10.3390/MA14216341.

[40] E. Widianto, Shobih, E.S. Rosa, K. Triyana, N.M. Nursam, I. Santoso, Performance analysis of carbon-based perovskite solar cells by graphene oxide as hole transport layer: Experimental and numerical simulation, Opt. Mater. (Amst). 121 (2021) 111584. https://doi.org/10.1016/J.OPTMAT.2021.111584.

[41] I. Montoya De Los Santos, H.J. Cortina-Marrero, M.A. Ruíz-Sánchez, L. Hechavarría-Difur, F.J. Sánchez-Rodríguez, M. Courel, H. Hu, Optimization of CH3NH3PbI3 perovskite solar cells: A theoretical and experimental study, Sol. Energy. 199 (2020) 198–205. https://doi.org/10.1016/J.SOLENER.2020.02.026.

[42] A.S. Chouhan, N.P. Jasti, S. Avasthi, Effect of interface defect density on performance of

perovskite solar cell: Correlation of simulation and experiment, Mater. Lett. 221 (2018) 150–153. https://doi.org/10.1016/J.MATLET.2018.03.095.

[43] P.N.A. Fahsyar, N.A. Ludin, N.F. Ramli, S. Sepeai, M.S. Suait, M.A. Ibrahim, M.A. Teridi, K. Sopian, Correlation of simulation and experiment for perovskite solar cells with MoS2 hybrid-HTL structure, Appl. Phys. A Mater. Sci. Process. 127 (2021) 1–10. https://doi.org/10.1007/S00339-021-04531-8/FIGURES/8.

[44] M. Burgelman, P. Nollet, S. Degrave, Modelling polycrystalline semiconductor solar cells, Thin Solid Films. (2000). https://doi.org/10.1016/S0040-6090(99)00825-1.

[45] F. Azri, A. Meftah, N. Sengouga, A. Meftah, Electron and hole transport layers optimization by numerical simulation of a perovskite solar cell, Sol. Energy. (2019). https://doi.org/10.1016/j.solener.2019.02.017.

[46] S. Karthick, O.M. Nwakanma, B. Mercyrani, J. Bouclé, S. Velumani, Efficient 2T CsKPb(IBr)3—Tin Incorporated Narrow Bandgap Perovskite Tandem Solar Cells: A Numerical Study with Current Matching Conditions, Adv. Theory Simulations. 4 (2021) 2100121. https://doi.org/10.1002/ADTS.202100121.

[47] S. Karthick, J. Bouclé, S. Velumani, Effect of bismuth iodide (BiI3) interfacial layer with different HTL's in FAPI based perovskite solar cell – SCAPS – 1D study, Sol. Energy. 218 (2021) 157–168. https://doi.org/10.1016/J.SOLENER.2021.02.041.

[48] F. Wang, S. Bai, W. Tress, A. Hagfeldt, F. Gao, Defects engineering for high-performance perovskite solar cells, 2 (2018) 22. https://doi.org/10.1038/s41528-018-0035-z.

[49] A. Maiti, S. Chatterjee, L. Peedikakkandy, A.J. Pal, Defects and Their Passivation in Hybrid Halide Perovskites toward Solar Cell Applications, Sol. RRL. 4 (2020) 2000505. https://doi.org/10.1002/SOLR.202000505.

[50] J.M. Ball, A. Petrozza, Defects in perovskite-halides and their effects in solar cells, Nat. Energy 2016 111. 1 (2016) 1–13. https://doi.org/10.1038/nenergy.2016.149.

[51] N. Singh, A. Agarwal, M. Agarwal, Numerical simulation of highly efficient lead-free all-perovskite tandem solar cell, Sol. Energy. (2020). https://doi.org/10.1016/j.solener.2020.08.003.

[52] A. Zekry, A. Shaker, M. Salem, Solar Cells and Arrays: Principles, Analysis, and Design, Adv. Renew. Energies Power Technol. 1 (2018) 3–56. https://doi.org/10.1016/B978-0-12-812959-3.00001-0.

[53] L. Et-taya, T. Ouslimane, A. Benami, Numerical analysis of earth-abundant Cu2ZnSn(SxSe1-x)4 solar cells based on Spectroscopic Ellipsometry results by using SCAPS-1D, Sol. Energy. (2020). https://doi.org/10.1016/j.solener.2020.03.070.

[54] S. Mahesh, J.M. Ball, R.D.J. Oliver, D.P. McMeekin, P.K. Nayak, M.B. Johnston, H.J. Snaith, Revealing the origin of voltage loss in mixed-halide perovskite solar cells, Energy Environ. Sci. (2020). https://doi.org/10.1039/c9ee02162k.

[55] W. Abdelaziz, A. Shaker, M. Abouelatta, A. Zekry, Possible efficiency boosting of non-fullerene acceptor solar cell using device simulation, Opt. Mater. (Amst). 91 (2019) 239–

245. https://doi.org/10.1016/J.OPTMAT.2019.03.023.

[56] W. Tress, M. Yavari, K. Domanski, P. Yadav, B. Niesen, J.P. Correa Baena, A. Hagfeldt, M. Graetzel, Interpretation and evolution of open-circuit voltage, recombination, ideality factor and subgap defect states during reversible light-soaking and irreversible degradation of perovskite solar cells, Energy Environ. Sci. 11 (2018) 151–165. https://doi.org/10.1039/C7EE02415K.

[57] D. Ompong, J. Singh, High open-circuit voltage in perovskite solar cells: The role of hole transport layer, Org. Electron. 63 (2018) 104–108. https://doi.org/10.1016/J.ORGEL.2018.09.006.

[58] H. Wang, A. Guerrero, A. Bou, A.M. Al-Mayouf, J. Bisquert, Kinetic and material properties of interfaces governing slow response and long timescale phenomena in perovskite solar cells, Energy Environ. Sci. 12 (2019) 2054–2079. https://doi.org/10.1039/C9EE00802K.

[59] N.A. Mahammedi, H. Gueffaf, B. Lagoun, M. Ferhat, Numerical simulation and optimization of a silicon clathrate-based solar cell n-Si136/p-Si2 using SCAPS-1D program, Opt. Mater. (Amst). 107 (2020) 110043. https://doi.org/10.1016/J.OPTMAT.2020.110043.

[60] M. Atowar Rahman, Enhancing the photovoltaic performance of Cd-free Cu2ZnSnS4 heterojunction solar cells using SnS HTL and TiO2 ETL, Sol. Energy. 215 (2021) 64–76. https://doi.org/10.1016/J.SOLENER.2020.12.020.

[61] S. Rahman, S.R. Al Ahmed, Photovoltaic performance enhancement in CdTe thin-film heterojunction solar cell with Sb2S3 as hole transport layer, Sol. Energy. 230 (2021) 605–617. https://doi.org/10.1016/J.SOLENER.2021.10.036.

[62] Q. Cang, H. Guo, X. Jia, H. Ning, C. Ma, J. Zhang, N. Yuan, J. Ding, Enhancement in the efficiency of Sb2Se3 solar cells by adding low lattice mismatch CuSbSe2 hole transport layer, Sol. Energy. 199 (2020) 19–25. https://doi.org/10.1016/J.SOLENER.2020.02.008.

[63] H. Baig, H. Kanda, A.M. Asiri, M.K. Nazeeruddin, T. Mallick, Increasing efficiency of perovskite solar cells using low concentrating photovoltaic systems, Sustain. Energy Fuels. 4 (2020) 528–537. https://doi.org/10.1039/C9SE00550A.

[64] A. Mahapatra, N. Parikh, P. Kumar, M. Kumar, D. Prochowicz, A. Kalam, M.M. Tavakoli, P. Yadav, Changes in the Electrical Characteristics of Perovskite Solar Cells with Aging Time, Mol. 2020, Vol. 25, Page 2299. 25 (2020) 2299. https://doi.org/10.3390/MOLECULES25102299.

[65] M. Becker, M. Wark, Sequentially Deposited Compact and Pinhole-Free Perovskite Layers via Adjusting the Permittivity of the Conversion Solution, Zeitschrift Fur Naturforsch. - Sect. A J. Phys. Sci. 74 (2019) 655–663. https://doi.org/10.1515/ZNA-2019-0141/PDF.

[66] R. Singh, S. Sandhu, J.J. Lee, Elucidating the effect of shunt losses on the performance of mesoporous perovskite solar cells, Sol. Energy. 193 (2019) 956–961. https://doi.org/10.1016/J.SOLENER.2019.10.018.

[67] D. Saranin, P. Gostischev, D. Tatarinov, I. Ermanova, V. Mazov, D. Muratov, A. Tameev, D. Kuznetsov, S. Didenko, A. Di Carlo, Copper Iodide Interlayer for Improved Charge Extraction and Stability of Inverted Perovskite Solar Cells, Mater. 2019, Vol. 12, Page 1406. 12 (2019) 1406. https://doi.org/10.3390/MA12091406.

[68] Z. Bi, S. Zhang, M. Thandapani, Y. Zhu, Y. Zheng, N.Q. Liem, X. Xiao, G. Xu, A. Guerrero, X. Xu, High Shunt Resistance SnO2-PbO Electron Transport Layer for Perovskite Solar Cells Used in Low Lighting Applications, Adv. Sustain. Syst. 5 (2021) 2100120. https://doi.org/10.1002/ADSU.202100120.

[69] S.H. Liu, E.J. Simburger, J. Matsumoto, A. Garcia, J. Ross, J. Nocerino, Evaluation of thin-film solar cell temperature coefficients for space applications, Prog. Photovoltaics Res. Appl. 13 (2005) 149–156. https://doi.org/10.1002/PIP.602.

[70] K.K. d. G. M.M. Finckenor, A researcher's guide to: space environmental effects., 2020. https://www.nasa.gov/sites/default/files/files/NP-2015-03-015-JSC_Space_Environment-ISS-Mini-Book-2015-508.pdf.

[71] J. Yang, Q. Bao, L. Shen, L. Ding, Potential applications for perovskite solar cells in space, Nano Energy. 76 (2020) 105019. https://doi.org/10.1016/J.NANOEN.2020.105019.

[72] Y. Tu, J. Wu, G. Xu, X. Yang, R. Cai, Q. Gong, R. Zhu, W. Huang, Perovskite Solar Cells for Space Applications: Progress and Challenges, Adv. Mater. 33 (2021) 2006545. https://doi.org/10.1002/ADMA.202006545.

[73] I. Cardinaletti, T. Vangerven, S. Nagels, R. Cornelissen, D. Schreurs, J. Hruby, J. Vodnik, D. Devisscher, J. Kesters, J. D'Haen, A. Franquet, V. Spampinato, T. Conard, W. Maes, W. Deferme, J. V. Manca, Organic and perovskite solar cells for space applications, Sol. Energy Mater. Sol. Cells. 182 (2018) 121–127. https://doi.org/10.1016/J.SOLMAT.2018.03.024.

[74] Z. Dong, W. Li, H. Wang, X. Jiang, H. Liu, L. Zhu, H. Chen, High-Temperature Perovskite Solar Cells, Sol. RRL. 5 (2021) 2100370. https://doi.org/10.1002/SOLR.202100370.

[75] M.A. Green, General temperature dependence of solar cell performance and implications for device modelling, Prog. Photovoltaics Res. Appl. (2003). https://doi.org/10.1002/pip.496.

[76] Y.H. Khattak, F. Baig, S. Ullah, B. Marí, S. Beg, H. Ullah, Enhancement of the conversion efficiency of thin film kesterite solar cell, J. Renew. Sustain. Energy. 10 (2018) 33501. https://doi.org/10.1063/1.5023478.

[77] L. Yu, A. Zunger, Identification of potential photovoltaic absorbers based on first-principles spectroscopic screening of materials, Phys. Rev. Lett. 108 (2012) 068701. https://doi.org/10.1103/PHYSREVLETT.108.068701/FIGURES/4/MEDIUM.

[78] J. Qian, Y. Liu, J. Song, L. Liu, B. Xu, G. Chen, W. Tian, Spectroscopic Limited Practical Efficiency (SLPE) model for organometal halide perovskites solar cells evaluation, Org. Electron. 59 (2018) 389–398. https://doi.org/10.1016/J.ORGEL.2018.05.056.

[79] S. Nazerdeylami, Dominant recombination mechanism in perovskite solar cells: A

theoretical study, Sol. Energy. 206 (2020) 27–34. https://doi.org/10.1016/J.SOLENER.2020.05.095.

[80] Q. Sun, H. Chen, W.J. Yin, Do Chalcogenide Double Perovskites Work as Solar Cell Absorbers: A First-Principles Study, Chem. Mater. 31 (2019) 244–250. https://doi.org/10.1021/ACS.CHEMMATER.8B04320/SUPPL_FILE/CM8B04320_SI_001.PDF.

[81] R. Chami, A. Lekdadri, L.H. Omari, E.K. Hlil, M. Chafi, Investigation of the photovoltaic properties of BaHf1-xZrxS3 (x≤1) chalcogenide perovskites using first principles calculations, Mater. Today Energy. 20 (2021) 100689. https://doi.org/10.1016/J.MTENER.2021.100689.